Heliyon 10 (2024) e23848

Contents lists available at ScienceDirect

Heliyon

journal homepage: www.cell.com/heliyon

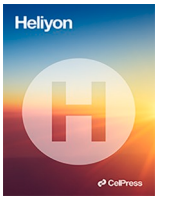

Unraveling the effect of Cu doping on the structural and morphological properties and photocatalytic activity of ZrO_2

Ibrahim M. Sharaf [a], J. Laifi [b], Shoroog Alraddadi [c], M. Saad [d], M.S.I. Koubesy [a], Nancy N. Elewa [e], Hussain Almohiy [d], Yasser M. Ismail [f,**], Alexander Soldatov [g], Abdelaziz M. aboraia [a,*]

[a] Physics Department, Faculty of Science, Al-Azhar University, Assiut Branch 71524, Egypt
[b] Physics Department, College of Science, Jouf University, P.O. Box 2014, Sakaka, Kingdom of Saudi Arabia
[c] Department of Physics, University College in AlJumum, Umm Al-Qura University, PO Box 715, Makkah 21955, Saudi Arabia
[d] Department of Radiological Sciences, College of Applied Medical Science, King Khalid University, Abha, Kingdom of Saudi Arabia
[e] Physics Department, Faculty of Science, Ain Shams University, Cairo, Egypt
[f] Department of Physics, Faculty of Science, Islamic University of Madinah, Kingdom of Saudi Arabia
[g] The Smart Materials Researcher Institute, Southern Federal University, Rostov on-Don, Russia

ARTICLE INFO

Keywords:
Nanoparticles
Photocatalysis
M.B.
RHB
Doping
Water purification

ABSTRACT

Pristine ZrO_2 and doped with different concentrations of Copper (0–7 %) were synthesized using a sol-gel combustion route. Several advanced techniques like XRD, EDX, TEM, XPS, P.L., and UV–vis spectrophotometer have characterized the compositions. The XRD proved that all peaks matched with a tetragonal phase of ZrO_2 without any impurities of other phases. An average crystallite size rises from 20 to 55 nm by increasing the concentrations of Copper. The elemental analysis was examined by EDX and confirmed the presence of Cooper, Zirconium, and Oxygen. The red shift was observed due to a decrease in the bandgap (5.5–4.01 eV) with increasing the Cu concentrations. From the analysis of photocatalysis of pure ZrO_2 and different concentrations of Cu-doped ZrO_2 for M.B., RHB, and mix of them. The increase in doping of Cu led to enhancing the performance of the removing MB from 35 to 80 %, however, the RHB degradation was from 42 to 81 % while the mix of M.B. and RHB reached 85 % with 7 % Cu-doping ZrO_2.

1. Introduction

Dyes remain used in various commercial initiatives for product leather, textiles, paper, cosmetics, plastics, and petrochemical manufacturing [1]. These many sectors create organic and inorganic contaminants and are pitched into water sources [2]. In addition, the tremendous rise in industrial development, agrochemical processes, and the overuse of non-renewable resources has also caused a severe decline in water resources [3]. Water pollution is the main issue affecting humans, plants, and animals. Thus, there is a solid motive to lessen environmental deterioration before the release of industrial waste [1–3].

The preservation of the environment is now a top concern for all nation's ecosystems [4]. Rhodamine B (RhB), a xanthene dye, and Methylene blue (M.B.), an organic and cationic dye, are two examples of dyes. Even though (RhB) and (M.B.) have a wide range of uses,

* Corresponding author.
** Corresponding author.
E-mail addresses: Yasser_ami@yahoo.com (Y.M. Ismail), a.m.aboraia@gmail.com, a.m.aboraia@azhar.edu.eg (A.M. aboraia).

https://doi.org/10.1016/j.heliyon.2023.e23848
Received 10 August 2023; Received in revised form 1 December 2023; Accepted 13 December 2023
Available online 18 December 2023

they are regarded as a type of water pollutants and organic dyes that can have detrimental effects on the environment [5,6]. Pollutant removal from wastewater, including dyes, nitrates, pesticides, etc., has taken on significant importance.

The scientific research community has employed a variety of methods to purge water of organic and inorganic contaminants, like bio-degradation [7], membranes process [8], ultrafiltration [9], coagulation [10], chlorination, ion exchange, advanced oxidation processes (AOP) [11], reverse osmosis [12], and so on. One of the most crucial methods is photocatalysis, which can entirely degrade dangerous pollutants to H_2O and CO_2. Photocatalysis happens after photons are absorbed on the surface of a semiconductor material, and then electron and hole pairs are produced. By interacting with H_2O, the produced electron-hole pairs cause oxidation and/or reduction. In this regard, photocatalysis is an exclusive and economical method that does not require particular conditions [13]. Currently, the decomposition of dyes by metal oxide can assist in effectively removing organic pollutants from wastewater.

One of these semiconductors is zirconia (ZrO_2), since it is widely employed in many applications due to its exceptional physio-chemical properties, being a safe element, resistant to high temperatures with good stability, and affordable and environmentally acceptable material [14]. Despite its broad bandgap (5.0–5.5 eV), ZrO_2 is active as a heterogeneous catalyst. ZrO_2 is a good candidate as a photocatalyst in some chemical processes due to its relatively wide bandgap "E_g" and C·B., which have a considerable negative value [15].

Due to zirconium dioxide's high band gap energy as the primary dielectric composition, it can absorb ultraviolet radiation only in the reaction of photocatalysis. In order to diminish the bandgap for the use of visible light employing a semiconductor, it is necessary to introduce a metal doping that could adjust the band gap of metal oxide semiconductors, which can introduce structural defects into the ZrO_2 structure and enhance visible-light photocatalytic [16]. One of the most inexpensive techniques is Sol-gel synthesis, which involves the conversion of a solution or sol into a solid gel network through a controlled chemical process. This versatile technique enables the synthesis of various materials with tailored properties, including ceramics, glasses, and nanoparticles. Sol-gel synthesis offers several advantages, including low processing temperatures, the ability to incorporate diverse materials, and the possibility of obtaining homogeneous and highly pure products. Additionally, it allows precise control over the structure and properties of the resulting materials, making it ideal for applications in fields such as optics, electronics, and biomedicine. The sol-gel process involves hydrolysis and condensation reactions of precursor compounds, followed by gelation and subsequent heating or drying to achieve the desired final product. Overall, sol-gel synthesis methods are widely utilized and appreciated for their versatility, controllability, and the wide range of materials that can be produced [17,18]. It is important to note that nanoparticles can be obtained by grinding the gel in specialized mills [19].

Introducing Copper can expand the lattice space, make structural defects, as well as extend the light absorption into the visible region. At the same time, the created structural defects further induce the optical properties of Cu/ZrO_2 nanocomposite with a single phase [20]. Adding these metals to the ZrO_2 decreases the bandgap of Cu–ZrO_2, which hinders the coupling of photo-excited electron-hole pairs of ZrO_2 [14].

Over Cu/ZrO_2 catalysts, Reddy et al. [15] and A. Fathy et al. [16] postulated a similar reaction mechanism. According to both experiments, a high dopant concentration outperforms pure and other dopant concentrations. They also emphasized the importance of the molecular interaction between Cu and Zr in comparison to other structural features. Zirconia nanostructures have recently been found to be capable of photocatalytically degrading aromatic molecules like dyes [14]. Moreover, photocatalytic usages of Zirconium oxide with CuO composition (spherical, 17–18 nm crystalline size) have been described; nevertheless, these applications have several drawbacks such as high concentration of photocatalyst for degradation, crystalline size, and U.V. as a light source [15,16]. However, the varied Energy gap of Ziconiumr oxide generally only absorbs light of UV [17,18]. Because of the large band gap energy of zirconia as the major dielectric component (the band gap energy has been observed in the range of 3.25 eV–5.1 eV), photocatalytic processes can only absorb U.V. irradiation. *P-n*-type heterojunction has been used for TiO2 in a wide range to lower the band gap for utilizing visible light by a semiconductor [8]. In this study, we synthesized a sequence of Cu-doped ZrO_2 nanoparticles with different concentrations (x = 0, 0.03, 0.05, and 0.07) mol% of Cu. The copper replacement was studied for its importance on optical, morphological, and structural properties, thus the photocatalytic activity. All the microstructures of the samples were investigated using X-ray diffraction (XRD) and transmission electron microscopy. Through the use of UV–Vis spectroscopy, the optical band gap was examined. The photocatalytic properties and applicability of $Zr_{1-x}Cu_xO_2$ nanoparticles for the degradation of M.B. and RhB and their mixtures in an aqueous medium have been studied. Our research will aid in converting industrial dyes into simpler, safer compounds and other environmental remediation techniques.

2. Experimental details

2.1. Synthesis of $Zr_{1-x}Cu_xO$

The sol-gel combustion technique prepared $Zr_{1-x}Cu_xO_2$ (x = 0, 0.03, 0.05, and 0.07) nanoparticles. We purchased all the chemicals we employed in our study from Sigma Aldrich: zinc nitrate, citric acetate, copper oxide, and DMF. The solution was fully mixed at room temperature while preserving the constant citric acid-to-metal cation ratio. The solution was placed under vigorous stirring at 150 °C then evaporated while frequently swirling until it formed a gel. After that, the gel precipitate underwent centrifugation and several rounds of washing with ethanol and distilled water. The yield was ground into a fine powder after being burned to 600 °C. A sol-gel combustion method has benefits more than other techniques owing to its easy fabrication, cheapness, and high efficiency [21]. Besides, due to its efficiency and sustainability, the combustion approach is fitting with the circular financial system.

2.2. Characterization

The synthesized nanoparticles employ a simple chemical sol-gel combustion route and are characterized by XRD using a Philips model PW 1710 with CuKα radiation ($\lambda = 1.5405$ Å), EDAX, and TEM). Transmittance spectra were determined using a double-beam spectrophotometer (JASCO 670 UV-VIS). The characteristics were measured from a range of 200–1000 nm. The photocatalytic ability of the obtained materials was studied using organic dyes-pollutants of rhodamine RhB and methylene blue M.B. The measurement of the photodegradability of the catalyst was evaluated using UV–visible spectroscopy.

2.3. The photocatalytic performance of $Zr_{1-x}Cu_xO$

The application of the synthesized materials was investigated by photodegradation of (RhB), (M.B.), and their mixture in the presence of U.V. irradiation in a photocatalytic chamber. The amount of the prepared $Zr_{1-x}Cu_xO_2$ catalyst in 20 mg was initially dissolved in 100 ml of standard rhodamine B, methylene blue, and their 50:50 mix in between, respectively, and then the solution mixture was stirred for 30 min in a dark state before radiation exposure to achieve an adsorption-desorption equilibrium. ZrO_2 adsorbed with dye molecules leads to a simple dye reaction with pairs of electrons and holes. The reaction mixture was finally irradiated at room temperature with a hero lab UV-15 S/L placed 10 cm above the solution mixture. The solution is continuously stirred in the air by a magnetic stirrer during irradiation. Every 10 min, 4 ml of dye solution was removed from the system for an hour and centrifuged. Its absorbance was measured using a UV–visible spectrophotometer to determine the percentage degradation. The photodegradation of the dyes was also evaluated by measuring the dye solution absorption at 665 nm. The following equation estimated the dye removal efficacy of photocatalytic [22]:

$$Removal\ \% = \frac{(C_o - C_t)}{C_o} \times 100 \tag{1}$$

After establishing the photocatalytic degradation mechanism, we obtained the initial and equilibrium pollutant concentrations (C_0 and C_t). The catalyst was then recovered through centrifugation and reused in the dye solution for recycling tests.

3. Discussion of the result

Fig. 1 (a) exhibits the XRD patterns of the pristine ZrO_2 and doped Cu samples. The pure phase of ZrO_2 and doped with different concentrations of Cu are a tetragonal phase with a space group $P4_2/nmc$:1 according to open crystallography data #210–0389 without any impurities of other phases. From phase analysis, it was noted that the Cu dissolved into the lattice of ZrO2 with changes in the original phase. Fig. 1 below shows the increase in the concentrations of dopant led to an increase in shifting at 2θ values in the lift direction. This change is essentially owing to the variance in ionic radii of Cu2+ and Zr4+; however, Cu2+ ions may also penetrate the host lattice via the substitution or interstitial mode, as previously reported [23].

The calculation of microstructure (size& stain), dislocation density and crystallites per unit area was computed according to Scherrer's equation since the crystalline size "D" [23]:

$$D = \frac{k\lambda}{\beta\ Cos\ \theta} \tag{2}$$

Since k = 0.9, λ is the Cu source and is equal to 1.54 nm, θ is the angle of diffraction, and β is the full width of the high maximum. The average crystalline size, microstrain $\varepsilon = \frac{\beta\ cos\ \theta}{4}$ [23], dislocation density and crystalline per unit are indexed in Table 1. The XRD confirmed the size increase by growing the Cu concentration, however, the microstrain decreased with an increase in the concentrations of Copper, as shown in Fig. 2. The increase in the Cu concentrations led to an increase in the peak intensity; this result indicates that the products are highly crystalline in nature, and these results match the reported data in Ref. [23].

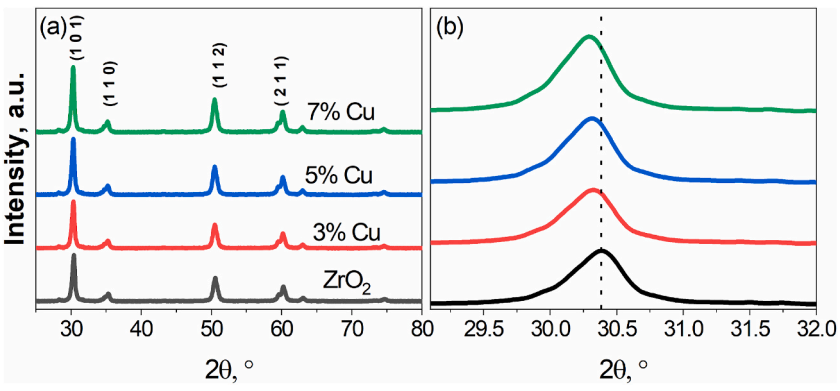

Fig. 1. (a) the XRD patterns of $Zr_{1-x}Cu_xO$ (x = 0,0.03,0.05 and 0.07) & the shift of peeaks on all samples (b).

Table 1
The average crystalline size, microstrain, dislocation density and crystalline per unit and band gap of $Zr_{1-x}Cu_xO$ (x = 0, 0.03, 0.05 and 0.07).

Samples	Size (nm)	Microstraine × 10^{-3}	Dislocation density × 10^{-3}	crystallites per unit area	Band gap, eV
ZrO_2	11.23	36.18	135.7081	923.34	5.5
0.03Cu-doped ZrO_2	12.22	35.96	135.63	933.30	5.4
0.05Cu-doped ZrO_2	15.43	6.89	5.6024	3.775	4.24
0.07Cu- doped ZrO_2	17.37	6.64	5.5406	3.787	4.01

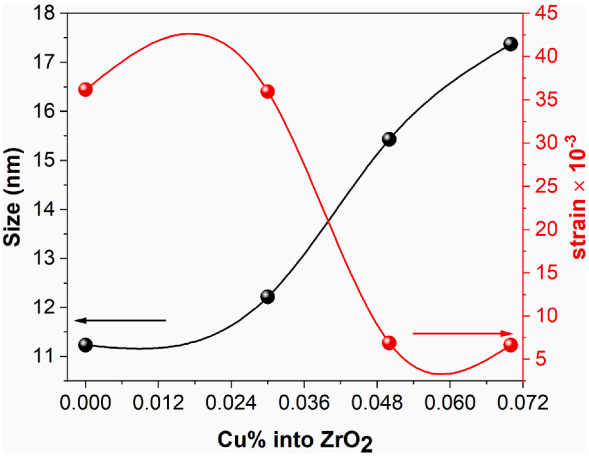

Fig. 2. The crystalline size and microstrain of Cu% doped ZrO_2.

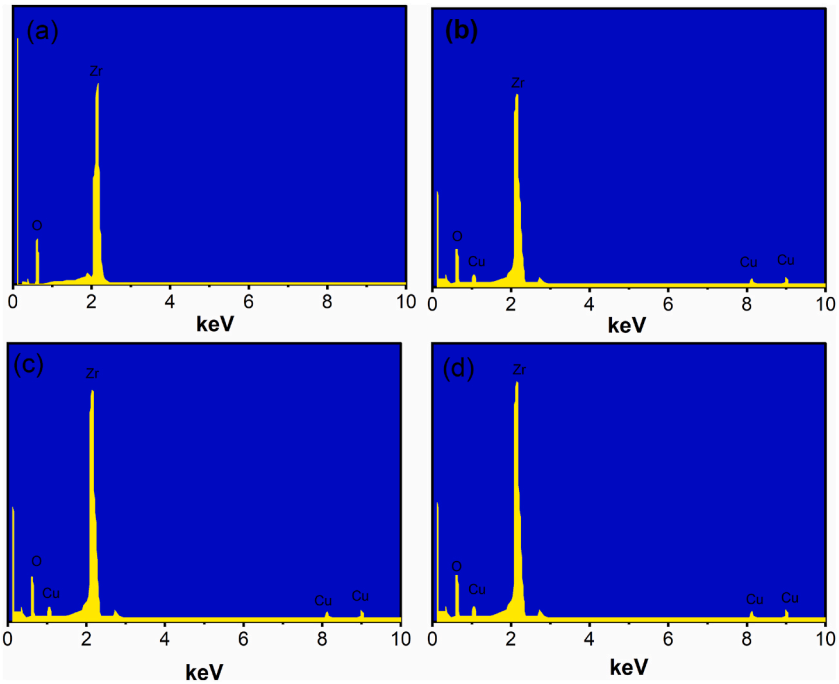

Fig. 3. The elemental analysis of ZrO_2 (a) 0.03 Cu doped ZrO_2 (b) 0.05 Cu doped ZrO_2 (c) 0.07 Cu doped ZrO_2 (d).

The elemental analysis has been done for all samples (undoped and oped ZrO_2) by EDAX and proved the presence of Cu concentrations and Zr according to Fig. 3(a–d).

3.1. Morphological properties

The morphological properties of pristine ZrO_2 and Copper doped ZrO_2 were examined with TEM, as demonstrated in Fig. 4(a–h). It is observed that the prepared samples in the nanoscale are spherical, and in different areas, there were some agglomerated owing to the preparation route. An average particle of all samples was computed by Image J, and it found that nanoparticles increased with increased concentrations of Copper from 20 to 55 nm since this increase may be attributed to the ionic radius of Cu being 140 pico; however the ionic radius of Zr was 0.08 nm thus the tendency for the crystallite size agglomeration to become bigger than the pristine one. The results match with XRD analysis.

3.2. Optical properties

Figure (5) exhibited the uv–vis spectra of absorption for all samples of undoped ZrO_2 and cu-doped ZrO_2, since the peak which appeared in the uv region owing to the electron charge transition from VB. to C.B. Additionally, a greater λ absorption edge of the band (redshift) is found in the doped samples, indicating that the optical band gap has been reduced, as exhibited by Fig. 5(b). The values of the optical energy gap were computed according to the intercept line based on the plots $(\alpha h\nu)^2$ on the y-axis and photon energy on the x-axis, as shown in Fig. 4(b). The estimated bandgap amounts are reported in Table 1. All of the optical analyses quantified the band gap amounts that were diminished from 5.5 to 4.01 eV with rising in the concentration of dopant from 0.03 to 0.07 mol %, nevertheless, the decrease in the Energy gap is due to d-d transition ($2T_{2g} \rightarrow 2A_{2g}$ or $2T_{1g}$), The Cooper ions demonstrated charge transfer within several ionic states of the host lattice, owing to many-body interactions and free charge carriers.

3.3. Analysis of XPS

XPS was utilized to examine the elemental composition and valence states of the samples, as shown in Fig. 6. In the undoped sample, Zr and O were the predominant elements, as indicated by the black line in Fig. 6. In the doped samples, the presence of Cu was observed in peaks (Cooper $2p_{3/2}$ & cooper $2p_{1/2}$) at 955 and 935 eV, signifying the divalent valence state of copper ions within the ZrO_2 lattice. The XPS analysis reveals a shift in binding energies to lower values with increasing dopant concentration. Zr 3 d electron state binding energies are noted at 183 eV and 185.2 eV, corresponding to Zirconiumr $3d_{5/2}$ and Zirconiumr $3d_{3/2}$ states, primarily indicating the presence of Zr^{4+} in the samples. The XPS spectrum of O1s displays a peak at around 530.7 eV, attributed to oxygen's lattice, confirming its −2 valence.

3.4. Analysis of the photoluminescence

Photoluminescence (PL) analysis is a vital technique for studying charge transport and electron-hole recombination in photocatalytic materials. In general, creating new levels of energy on the surface of ZrO_2 due to the transition of electrons from the CB to VB results in PL emission. Fig. 7 shows PL emission spectra of pure ZrO_2 (black line) and Cu-doped ZrO_2 with concentrations of 3 %, 5 %,

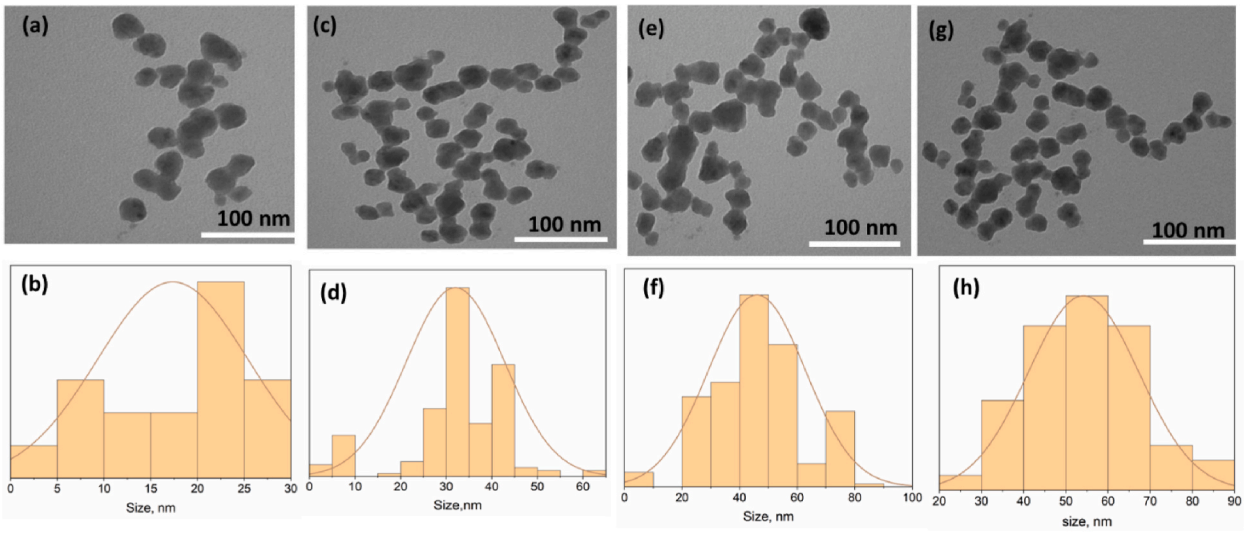

Fig. 4. The photo's TEM ZrO_2 and TEM analysis (a,b), 3 % Cu doped ZrO_2 and TEM analysis (c,d) 5 % Cu doped ZrO_2 and TEM analysis (e,f) 7 % Cu doped ZrO_2 and TEM analysis (g,h).

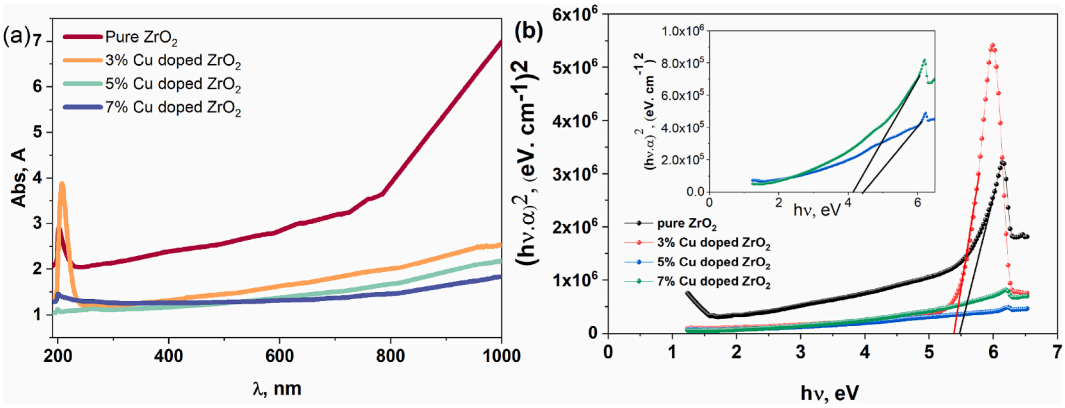

Fig. 5. (a) The uv–vis absorption spectrum of $Zr_{1-x}Cu_xO$, (b) Tauc's plot of pristine ZrO_2 and different Cu concentrations doped Zirconium oxide.

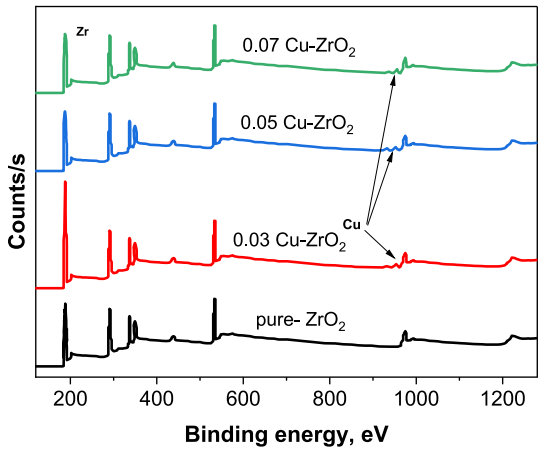

Fig. 6. XPS spectra survey of the as-synthesized samples.

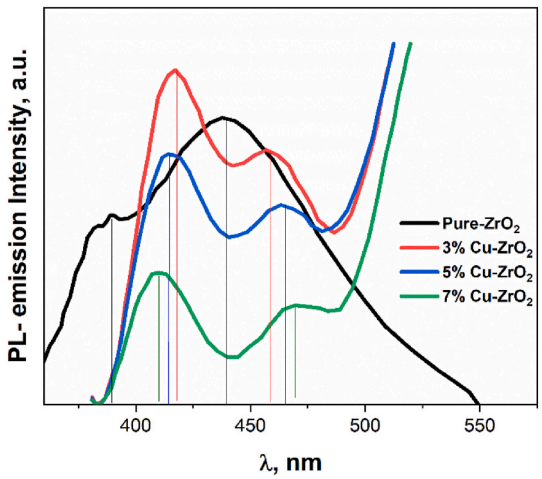

Fig. 7. The photoluminescence of $Zr_{1-x}Cu_xO_2$ (x = 0, 0.03, 0.05 and 0.07).

and 7 % (red, blue, and green lines, respectively) nanoparticles under excitation at $\lambda = 350$ nm. The emission peaks are observed at 388, 408, 413, 438, 457, and 467 nm. The emission at 388 nm is attributed to ionized oxygen vacancies from the CB of ZrO_2, while vacancies of Zr are detected at 408, 413, and 438 nm. These bands are related to band edge emissions resulting from free-exciton

recombination. The peaks at around 457 and 467 nm are associated with mid-gap trap states, such as surface defects. The PL analysis suggests the presence of Zr–O complexes associated with defects, and the reduced intensity of PL emissions in copper-doped ZrO_2 indicates decreased charge separation of electron-hole pairs. Notably, as shown in Fig. 7, sample 7 % Cu-doped ZrO_2 exhibits the lowest PL emission intensity, likely due to the dispersion of Cu^{2+} on the ZrO_2 surface, which effectively demotes the electron-hole pairs recombination, leading to improved photocatalytic activity.

3.5. BET analysis

BET surface analysis was used to analyze the surface properties of the photocatalysts, and the findings are displayed in Fig. 8. The loops of the hysteresis are detected at rather high pressure, indicating that the materials have a mesoporous structure. According to the IUPAC description, all of the materials are fourth-type isotherms with H_2 hysteresis loops. Brunauer Emmett Teller (BET) and Barrett Joyner Halenda (BJH) isotherms were used to determine the specific surface area, distribution of pore size, and volume. Because of the action of Cooper-oxygen clusters on the surface, the undoped sample had a higher specific surface area (SSA), pore volume and size than the 0.07 Cu incorporated in the Zr sample.

3.6. Photocatalytic performance

Photogeneration of electrons and holes is required for good photocatalytic activity. Only photons with energies bigger than the photocatalyst's energy gap can generate photo electron holes. If we utilize sunlight as the source, a rise in the energy gap suggests that a certain section of the spectrum is no longer effective for photoelectron-hole formation, and the photocatalytic activity is hampered. If the incident photon energy exceeds the photocatalyst's energy gap and the material is thermally sensitive, the excess incident energy is transformed into heat and plays a role in determining photocatalytic activity. Nanoscale features that promote the transport of electrons and holes generated within crystals to the surface can improve photocatalytic activity. The surface composition of ZrO_2 is also significant in dye adsorption and thus, photocatalytic activity. Apart from pure-ZrO_2, oxygen vacancies also play an important role in dye photodegradation. Specifically, surface oxygen vacancies can act as photoinduced charge traps and adsorption sites, allowing charge to transfer to adsorbed compounds and preventing recombination of photogenerated charge carriers, resulting in improved photocatalytic performance.

Fig. 9 depicts the temporal changes in the absorbance spectra of M.B. dye using (a) undoped ZrO_2 nanoparticles and (b, c and d) Cu-doped ZrO_2 nanoparticles. The peaks around 665 nm as demonstrated in Fig. 9 correspond to the significant absorption of M.B. dye. The MB solution is loaded with photocatalysts and agitated for 30 min in the dark. The readily available charge carriers initially participate in the catalytic action, resulting in very minor degradation. Then irradiate the dye for 1 h under sunlight and around 35 % of M.B. has been degraded. However the increase in the Cu doping with ZrO_2 led to enhance the photocatalytic performance of ZrO_2 catalytic from 35 to 80 %, as shown in Fig. 9(a–d)

In the same way, all these samples used as catalysts to remove the RHB dye and it found that the efficiency of removal degradation increased by increasing the incorporation of Cu concentrations since the efficiency of removing the RHB dye was 42 for pure ZrO_2, however the increase in the doping of Cu led to enhance photocatalytic activity to 81 %, as shown in Fig. 10(a–d). On the other hand, water maybe consists of more than one dye or mix of them, so we mix RHB and M.B., then the activity of photocatalytic was tested and found the removal efficiency was 85 for M.B. and more than 75 % of RHB, as seen in Fig. 11.

Fig. 12(a) illustrates the photocatalysts' dye degradation percentage. Even after 60 min in the photocatalyst's presence, no significant dye colour was identified in pristine zirconium oxide; only 33 % of the dye was destroyed, which may possibly be owing to freely existing charge carriers. Within 60 min of light irradiation, 35 %, 70.6 %, and 81.4 % of M.B. dye degradations were seen in 0.03, 0.05, and 0.07 Cu incorporated to Zr catalyst, correspondingly. On the other hand, in RHB as demonstrated Fig. 12 b, the degradation was 58 %, 43, 48, and 82 % of RHB dye degradations were seen 0.03, 0.05, and 0.07 Cu incorporated to Zr catalyst, correspondingly.

The computed rate constants from the slope are 0.00634, 0.0068, 0.00174 and 0.0289 min^{-1} for pure, 0.03, 0.05, and 0.07 Cu incorporated into Zr catalyst, correspondingly. The adjusted concentration of Cu was 0.007 incorporated into the Zr sample, displayed a greater degradation rate constant of M.B. than the other samples, as demonstrated in Fig. 13(a). However, the rate constants for RHB were 0.0239, 0.0143,0.00908 and 0.0112 min^{-1}, as demonstrated in Fig. 13(b).

4. Conclusion

Pristine ZrO_2 and doped with different concentrations of Copper (0–7 %) were synthesized using a sol-gel combustion route. The XRD proved that all peaks matched with a tetragonal phase of ZrO_2 without any impurities of other phases. The TEM has determined an average crystallite size rises from 20 to 55 nm by increasing the concentrations of Copper. The elemental analysis was examined by EDX and confirmed the presence of Cooper, Zirconium, and Oxygen. The red shift was observed due to a decrease in the bandgap (5.5–4.01 eV) with increasing the Cu concentrations. BET surface analysis was used to analyze the surface properties of the photocatalysts. The hysteresis loops are detected at rather high pressure, indicating that the materials have a mesoporous structure. According to the IUPAC description, all of the samples are fourth-type isotherms with H_2 hysteresis loops. Brunauer Emmett Teller (BET) and Barrett Joyner Halenda (BJH) isotherms were used to determine the specific surface area (SSA), distribution of pore size, and volume. Because of the action of Cu–O clusters on the surface, the undoped sample had a higher specific surface area, pore size, and pore volume than the 0.07 Cu–Zr sample. From the analysis of photocatalysis of pure ZrO_2 and different concentrations of Cu-doped ZrO_2 for M.B., RHB, and mix of them. The increase in doping of Cu led to enhancing the performance of the removing MB from 35 to 80

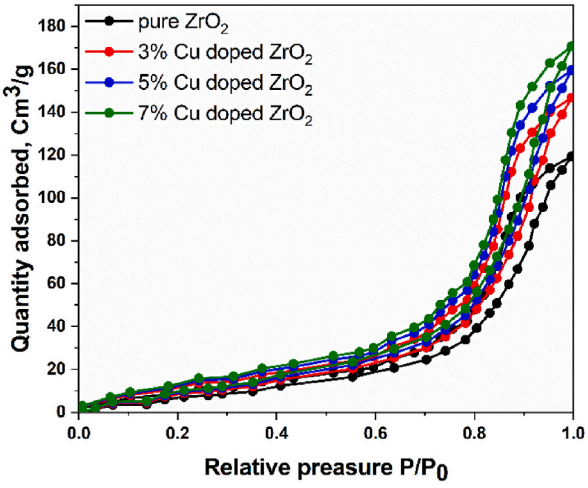

Fig. 8. N_2 adsorption–desorption isotherms of the synthesized materials.

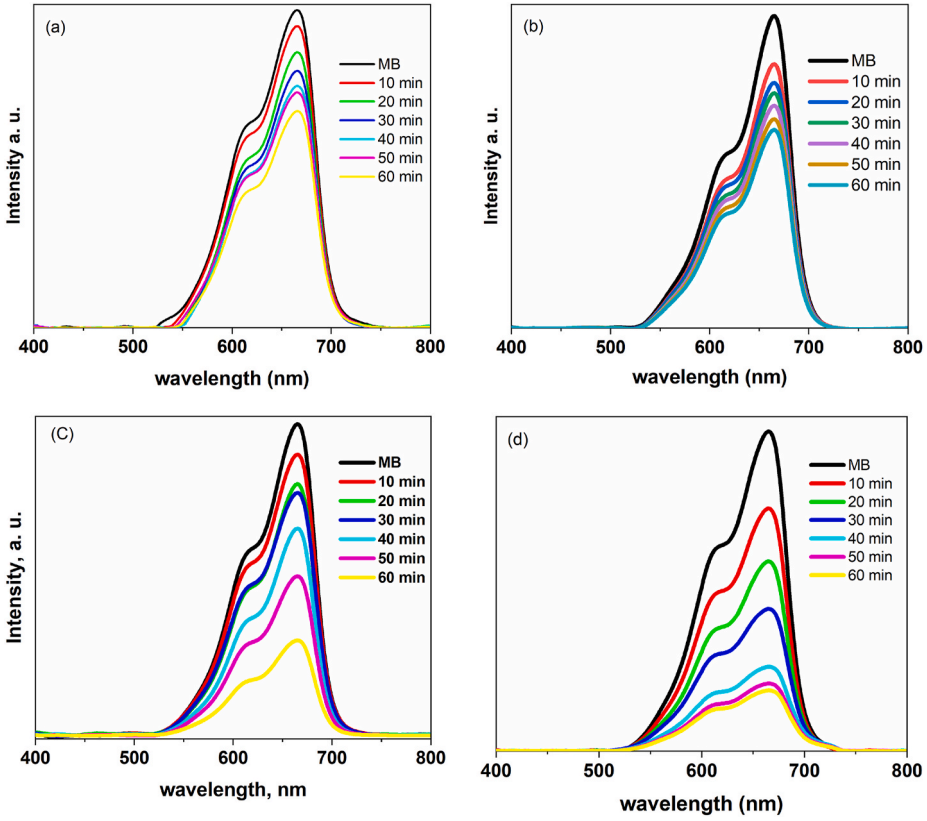

Fig. 9. The photodegradation of $Zr_{1-x}Cu_xO$ x = 0 (a), x = 0.03(b), x = 0.05(c), and x = 0.07(d) for MB.

%, however, the RHB degradation was from 42 to 81 % while the mix of M.B. and RHB reached 85 % with 7 % Cu-doping ZrO_2. The adjusted concentration of Cu was 0.007 incorporated into the Zr sample, displaying an imposing degradation rate constant of M.B. than the other samples according to the calculated kinetics rate constant.

Data availability statement

Has data associated with your study been deposited into a publicly available repository?

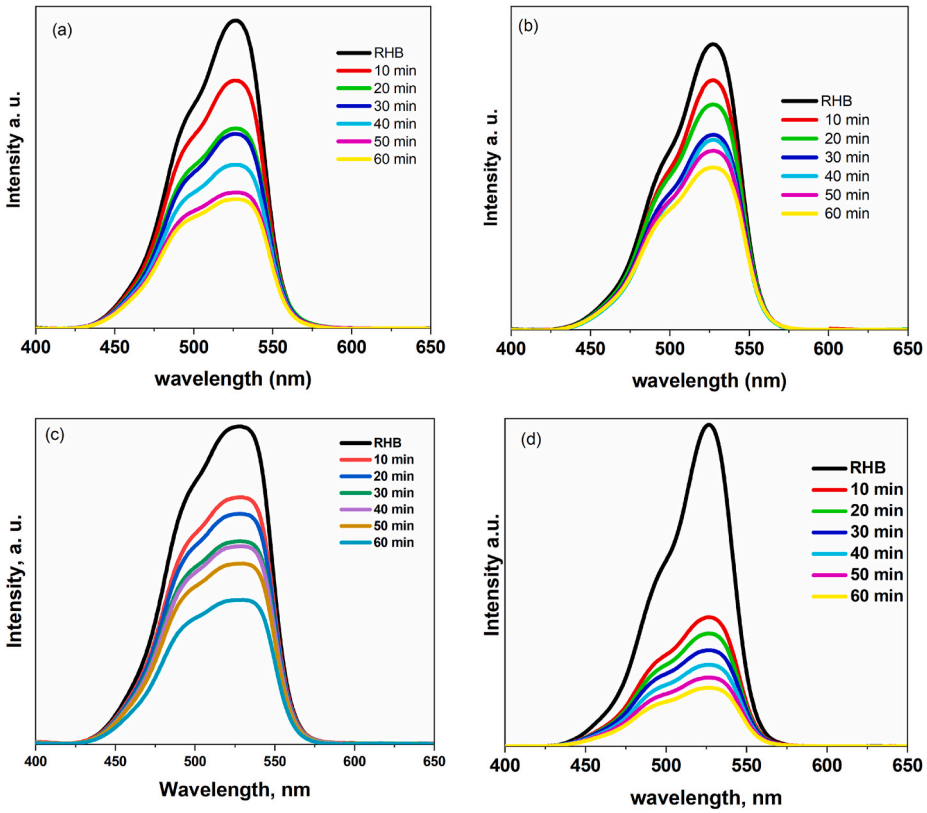

Fig. 10. The photodegradation of $Zr_{1-x}Cu_xO$ x = 0 (a), x = 0.03(b), x = 0.05(c), and x = 0.07(d) for RHB.

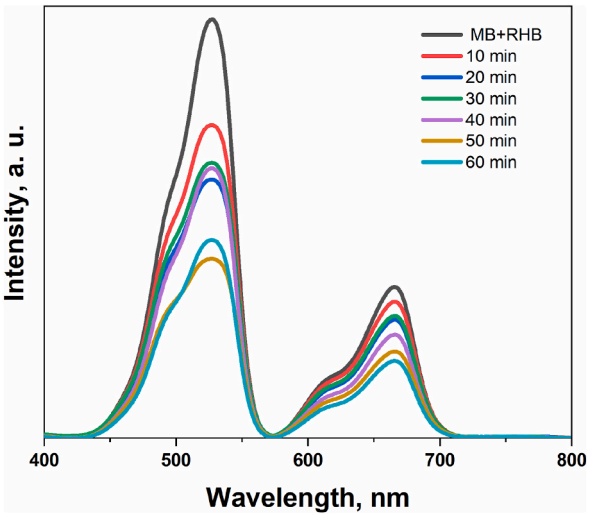

Fig. 11. The photodegradation of $Zr_{93}Cu_{0.07}O$ for Mix dyes of RhB + MB.

No.
Please select why.
Data will be made available on request.

CRediT authorship contribution statement

Ibrahim M. Sharaf: Writing - original draft, Methodology, Data curation. **J. Laifi:** Investigation, Formal analysis, Data curation.

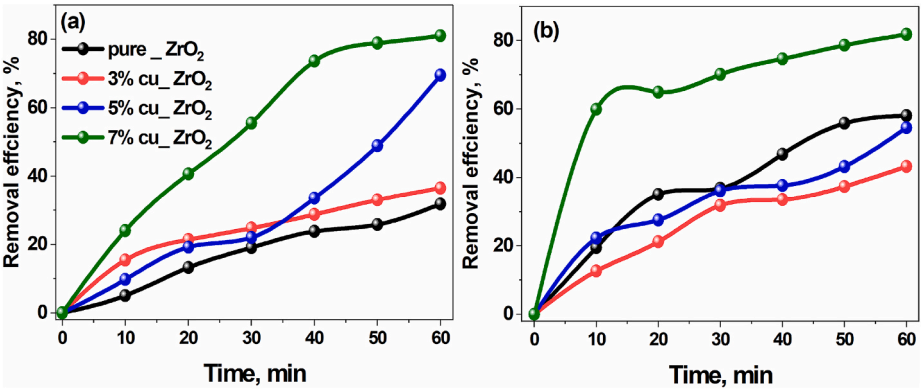

Fig. 12. The removal efficiency of (a) M.B. &(b) RHB.

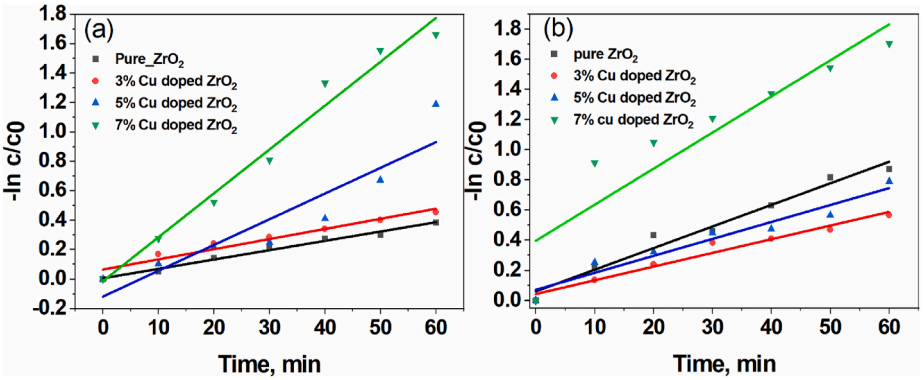

Fig. 13. Kinetics of catalytic degradation for (a) M.B. and (b) RHB.

Shoroog Alraddadi: Visualization, Validation, Methodology, Investigation, Data curation. **M. Saad:** Writing - review & editing, Supervision, Resources, Methodology, Conceptualization. **M.S.I. Koubesy:** Validation, Methodology, Formal analysis, Conceptualization. **Nancy N. Elewa:** Visualization, Validation, Project administration, Investigation. **Hussain Almohiy:** Writing - original draft, Supervision, Resources, Project administration, Investigation. **Yasser M. Ismail:** Writing - original draft, Validation, Methodology, Investigation, Formal analysis. **Alexander Soldatov:** Visualization, Validation, Supervision, Investigation. **Abdelaziz M. aboraia:** Writing - review & editing, Writing - original draft, Visualization, Validation, Methodology, Investigation, Data curation.

Declaration of competing interest

The authors declare that they have no known competing financial interests or personal relationships that could have appeared to influence the work reported in this paper.

Acknowledgment

The authors extend their appreciation to the Deanship of Scientific Research at King Khalid University for funding this work through large group Research Project under grant number RGP2/289/44.

References

[1] G. Liu, et al., Synergistic effects of B/N doping on the visible-light photocatalytic activity of mesoporous TiO2, Angew. Chem. Int. Ed. 47 (24) (2008) 4516–4520.
[2] J. Shi, et al., Pollution control of wastewater from the coal chemical industry in China: environmental management policy and technical standards, Renew. Sustain. Energy Rev. 143 (2021), 110883.
[3] Z. Gan, et al., Mechanical properties of zirconia thin films deposited by filtered cathodic vacuum arc, J. Am. Ceram. Soc. 88 (8) (2005) 2227–2229.
[4] M. Pavel, et al., Photocatalytic degradation of organic and inorganic pollutants to harmless end products: assessment of practical application potential for water and air cleaning, Catalysts 13 (2) (2023) 380.
[5] S. Harish, et al., Interface enriched highly interlaced layered MoS 2/NiS 2 nanocomposites for the photocatalytic degradation of rhodamine B dye, RSC Adv. 11 (31) (2021) 19283–19293.
[6] A.H. Kianfar, M.A. Arayesh, M.M. Momeni, Degradation of MB and RhB by modified ZrO 2 nanoparticles via sunlight, Appl. Phys. A 127 (2021) 1–9.

[7] V. Hasirci, N. Hasirci, Fundamentals of Biomaterials, Springer, 2018.
[8] H. Qin, et al., Preparation of yttria-stabilized ZrO2 nanofiltration membrane by reverse micelles-mediated sol-gel process and its application in pesticide wastewater treatment, J. Eur. Ceram. Soc. 40 (1) (2020) 145–154.
[9] K. Saeed, et al., Synthesis, characterization, and photocatalytic application of Pd/ZrO 2 and Pt/ZrO 2, Appl. Water Sci. 8 (2018) 1–6.
[10] M. Campinas, et al., Adsorption/coagulation/ceramic microfiltration for treating challenging waters for drinking water production, Membranes 11 (2) (2021) 91.
[11] Y. Deng, R. Zhao, Advanced oxidation processes (AOPs) in wastewater treatment, Current Pollution Reports 1 (2015) 167–176.
[12] K.P. Lee, T.C. Arnot, D. Mattia, A review of reverse osmosis membrane materials for desalination—development to date and future potential, J. Membr. Sci. 370 (1–2) (2011) 1–22.
[13] G. Rajesh, et al., Enhancement of photocatalytic activity of ZrO 2 nanoparticles by doping with Mg for UV light photocatalytic degradation of methyl violet and methyl blue dyes, J. Mater. Sci. Mater. Electron. 31 (2020) 4058–4072.
[14] W.R.L.N. Bandara, et al., Is nano ZrO 2 a better photocatalyst than nano TiO 2 for degradation of plastics? RSC Adv. 7 (73) (2017) 46155–46163.
[15] E.-S.R. Khattab, et al., Band structure engineering and optical properties of pristine and doped monoclinic zirconia (m-ZrO2): density functional theory theoretical prospective, ACS Omega 6 (44) (2021) 30061–30068.
[16] A. Fathy, O. Elkady, A. Abu-Oqail, Synthesis and characterization of Cu–ZrO2 nanocomposite produced by thermochemical process, J. Alloys Compd. 719 (2017) 411–419.
[17] M. Sohaib, et al., Novel sol–gel synthesis of Mo-doped ZnO-NPs for photo-catalytic waste water treatment using the RhB dye as a model pollutant, Environ. Dev. Sustain. 25 (10) (2023) 11583–11598.
[18] T. López, et al., ZrO 2 and Cu/ZrO 2 sol–gel materials spectroscopic characterization, J. Sol. Gel Sci. Technol. 33 (2005) 93–97.
[19] D. Bokov, et al., Nanomaterial by sol-gel method: synthesis and application, Adv. Mater. Sci. Eng. 2021 (2021) 1–21.
[20] A. Fathy, A. Wagih, A. Abu-Oqail, Effect of ZrO2 content on properties of Cu-ZrO2 nanocomposites synthesized by optimized high energy ball milling, Ceram. Int. 45 (2) (2019) 2319–2329.
[21] H. Singh, et al., Tuning the bandgap of m-ZrO2 by incorporation of copper nanoparticles into visible region for the treatment of organic pollutants, Mater. Res. Bull. 123 (2020), 110698.
[22] C.V. Reddy, et al., Copper-doped ZrO2 nanoparticles as high-performance catalysts for efficient removal of toxic organic pollutants and stable solar water oxidation, J. Environ. Manag. 260 (2020), 110088.
[23] H.-d. Zhuang, et al., Structure and performance of Cu/ZrO2 catalyst for the synthesis of methanol from CO2 hydrogenation, J. Fuel Chem. Technol. 38 (4) (2010) 462–467.